RSC Advances

PAPER

View Article Online
View Journal | View Issue

Cite this: *RSC Adv.*, 2016, **6**, 110629

Tailored activated carbons for supercapacitors derived from hydrothermally carbonized sugars by chemical activation†

Kian Keat Lee,[a] Wenming Hao,[a] Mikaela Gustafsson,[a] Cheuk-Wai Tai,[a] Daniel Morin,[b] Eva Björkman,[c] Malte Lilliestråle,[c] Fredrik Björefors,[d] Anna M. Andersson*[b] and Niklas Hedin*[a]

Received 30th September 2016
Accepted 13th November 2016

DOI: 10.1039/c6ra24398c

www.rsc.org/advances

Activated carbons (ACs) are actively researched as electrode materials for supercapacitors and there is a significant interest to produce ACs from sustainable and low cost precursors. In this study, various ACs were prepared from hydrothermally carbonized sugars by KOH activation. Both the hydrothermal carbonization and activation processes were optimized to tailor the properties (*e.g.* textural properties, chemical composition, N-doping, electrical conductivity) of the ACs. For instance, the Brunauer–Emmett–Teller (BET) surface areas (S_{BET}) were tuned in the range of 800–3000 $m^2\ g^{-1}$ with associated variation in the extent of microporosity and pore size distributions (PSDs). The ACs were evaluated electrochemically as materials for supercapacitor electrodes in a symmetrical two-electrode cell using an aqueous electrolyte. The relationship between the electrochemical, textural, electrical, and physicochemical properties were analyzed systematically to understand the key factors determining the electrochemical performance. A high specific capacitance (C_m) of ~260 F g^{-1} was achieved at a moderately high S_{BET} of ~1300 $m^2\ g^{-1}$, which was equivalent to a C_m/S_{BET} of 20 μF cm^{-2}, for an optimal AC prepared from hydrothermally carbonized glucose. The very high surface-specific capacitance highlights that the specific surface area is certainly not the sole limiting parameter for effective electrode materials.

1. Introduction

Supercapacitors (or ultracapacitors) are electrochemical energy storage devices that store electricity electrostatically or electrochemically *via* redox reactions and electrosorption. Hence, they are closely related to batteries.[1–4] With their high energy densities of >10 kW h kg, and discharge times that are in the range of milliseconds to minutes, many applications in the previously void region between conventional capacitors and batteries are enabled. For electrified vehicles, applications could be in regenerative braking systems, start–stop systems, and in power boosts for various driver interfaces such as facilitated steering or air conditioning.[4–6] Since batteries and supercapacitors in many cases are complimentary, hybrid systems of both technologies are often judged to be attractive.[2,5] The hybrid systems are suggested for large-scale energy storage to enable effective power compensation in electrical grids. Such a combined storage features short and long time scale compensation and is potentially very beneficial from a cost perspective.[5]

Highly porous carbons are the primary choice of electrode materials for supercapacitors. This preference relates to their high specific surface area or high (ultra)micropore volume, which is necessary for a high electric double layer (EDL) capacitance; to their relatively high electrical conductivity, which is important for the power delivery; and to their low production cost, which is critical for industrial applications.[1] By rationally tuning the textural, structural, and surface properties of carbon materials, optimum electrochemical performance can be achieved and adapted based on system requirements. Considering sustainability and economy, it is preferred that ACs are produced from renewable, sustainable, abundant and cost-

[a]*Department of Materials and Environmental Chemistry-Arrhenius Laboratory, Stockholm University, SE-106 91 Stockholm, Sweden. E-mail: niklas.hedin@mmk.su.se*
[b]*ABB Corporate Research, Forskargränd 7, SE-721 78 Västerås, Sweden. E-mail: anna.m.andersson@se.abb.com*
[c]*Biokol Lilliestråle & Co KB, Sibyllegatan 53, SE-114 43 Stockholm, Sweden*
[d]*Department of Chemistry-Ångström Laboratory, Uppsala University, Box 538, SE-751 21 Uppsala, Sweden*

† Electronic supplementary information (ESI) available: Comparison of C_m values calculated from voltage ranges of 0 to 1 V, 0 to 0.9 V and 0 to 0.8 V; test set-up for measuring electrical conductivity; TGA of HTC-GA and HTC-G, N_2 adsorption–desorption isotherms for AC-GFe-800-2h and AC-GFe-800-4h; XPS wide spectra and high-resolved C 1s spectra; relationship between the activation temperature and bulk elemental composition of ACs; XRD patterns; galvanostatic charge–discharge curves; CV curves at different scan rates; electrical conductivity of AC powders; cycling life time; Raman spectra; SEM, TEM, HRTEM, BF-STEM and HAADF-STEM images; EELS. See DOI: 10.1039/c6ra24398c

effective resources. Carbohydrate-based ACs fit these demands as they can be manufactured reproducibly at scale from consistent and abundant sources. Hence, they are up-and-coming alternatives.[7–10]

Hydrothermal carbonization of biomasses and sugars produce hydrothermal carbons, at low temperatures (150–250 °C) and autogenous pressure.[11] These hydrothermal carbons are suitable precursors to ACs. Compared with precursors produced by conventional pyrolysis, the energy cost of producing hydrothermal carbons is lower. This difference relate to the lower temperature, exothermic reactions, and no need for precursor drying.[11–13] Moreover, the hydrothermal carbonization process is capable of homogenizing biomass precursors, removing certain mineral impurities, and providing an excellent carbon yield.[14] The hydrothermal carbons often display uniform physico-chemical properties and various tunable functional groups (*e.g.* oxygen, nitrogen, phosphorus) that depend on the composition of the biomass, additives and the process conditions.[15–18]

As a simple form of hydrothermal carbon, hydrothermally carbonized glucose (HTC-glucose), has been increasingly studied since the early 2000s.[11,19,20] The microspheres of HTC-glucose generally possess almost no open porosity, and post-heat treatment only leads to a moderately increased surface area (400 $m^2\ g^{-1}$).[19] Hence, activation procedures are indispensable to generate highly porous ACs. ACs have been prepared from HTC-glucose by both physical activation (*e.g.* CO_2 (ref. 10 and 21) and air[22]) and chemical activation (*e.g.* H_3PO_4,[21] NaOH[21] and KOH[14,21,23–27]). KOH activation is advantageous in terms of lower activation temperature, shorter activation time and higher yield.[28] More importantly, this method is specifically advantageous for producing ACs for supercapacitors because of their well-defined pore size and PSD, tunable surface area and (ultra) micropore volume, and high electrical conductivity.[29,30]

Sevilla *et al.* compared the physico-chemical and electrochemical properties of ACs prepared by KOH activation of glucose and HTC-glucose.[14] Using HTC-glucose, the AC yield was doubled and a significantly improved rate capability was observed for the AC-based electrodes. Recently, Sevilla *et al.* further optimized the KOH-ACs derived from HTC-glucose and increased the S_{BET} from 1510 to 2950 $m^2\ g^{-1}$, the total pore volume (V_t) from 0.68 to 1.36 $cm^3\ g^{-1}$, and the micropore volume ($V_{DR\text{-}N_2}$, based on Dubinin-Radushkevich (DR) method) from 0.60 to 1.02 $cm^3\ g^{-1}$. The optimized ACs displayed a C_m of 320 F g^{-1} in a two-electrode set up with a 1 M H_2SO_4 electrolyte.[24] Notably, several other groups have prepared KOH-ACs from HTC-glucose with various degree of success when it comes to the specific capacitance (C_m). Gao *et al.* observed a C_m of 58 F g^{-1} in a 6 M KOH electrolyte for an AC with a S_{BET} of 1197 $m^2\ g^{-1}$, a V_t of 0.74 $cm^3\ g^{-1}$ and a $V_{\mu p\text{-}t}$ (micropore volume, based on *t*-plot method) of 0.48 $cm^3\ g^{-1}$.[25] Salinas-Torres *et al.* observed a C_m of 125 F g^{-1} in a 0.5 M H_2SO_4 electrolyte for an AC with a S_{BET} of 1766 $m^2\ g^{-1}$ and $V_{DR\text{-}N_2}$ of 0.58 $cm^3\ g^{-1}$.[26] Zheng *et al.* observed a C_m of 240 F g^{-1} in a 6 M KOH electrolyte for an AC with S_{BET} of 2633 $m^2\ g^{-1}$, a V_t of 1.86 $cm^3\ g^{-1}$, and a $V_{\mu p\text{-}t}$ of 0.58 $cm^3\ g^{-1}$.[27] Collectively this spread of values indicates that the C_m is strongly related to the textural properties of the ACs but also to other less obvious relations.

HTC-glucosamine has also been studied as a precursor of ACs for electrodes of supercapacitors.[31] Glucosamine relates to the abundant chitin making it a viable and sustainable option. Hydrothermal carbonization of N-containing precursors is a straightforward process to enrich the carbonized products with N-containing moieties.[15] This approach appears to be more straightforward than treating the precursors with ammonia or urea.[32,33] N-Doped carbons also appear to have improved conductivities and enhanced capacitances due to redox reactions of electrochemically active nitrogen functional groups.[32,34,35]

Iron species (*e.g.* iron-oxide nanoparticles, $Fe(NH_4)_2(SO_4)_2$, $FeSO_4 \cdot 7H_2O$, $FeCl_2 \cdot 4H_2O$, $Fe_2(SO_4)_3$) have been used as catalysts or additives in hydrothermal carbonization of biomasses.[36–38] Cui *et al.* reported that the Fe^{2+} ions from $Fe(NH_4)_2(SO_4)_2$ and related iron-oxide nanoparticles can effectively catalyze the hydrothermal carbonization of starch and rice grains.[37] Such Fe^{2+} ions and iron-oxide nanoparticles were ascribed structure-directing effects forming hollow microspherical and rope-like carbon-rich nanostructures, respectively. Nanoparticles of magnetic iron[38] or iron oxide[36] have been embedded in hydrothermal carbons and the corresponding ACs. The latter case prompts further curiosity in relation to supercapacitors as iron compounds demonstrated redox capacitance[39,40] and potentially magnetic-field-enhanced capacitance.[41]

When designing optimal ACs for supercapacitor electrodes, it is crucial to understand the role of different types of porosity on the formation of EDL capacitance. Recent discoveries have shown that there is no simple linear correlation between the BET specific surface area (S_{BET}) and capacitance, especially when the S_{BET} is >1500 $m^2\ g^{-1}$, but rather stressed the importance of optimal micropore size, pore size uniformity and pore connectivity.[42] It has been proposed that ACs with very high S_{BET} have too thin pore walls that are unable to screen completely the fields of ions in adjacent pores.[43] Benchmarking studies by Gogotsi, Simon and co-workers revealed that the pores with a width of <1 nm, and close to the size of electrosorbed ions, are the most optimum for EDL formation in non-aqueous electrolyte.[44–46] This new theory was further supported by Béguin's group, for both aqueous and non-aqueous electrolytes.[47,48]

Here, we present a systematic and comprehensive study where the textural properties (porosity, pore size, PSD *etc.*) of KOH-ACs derived from HTC-sugars (glucose and glucosamine) were tailored with respect to their performance as electrodes in supercapacitors. HTC-glucosamine was used to study the effect of N doping. In addition, the possible incorporation and effect of iron species from $FeSO_4 \cdot 7H_2O$ were investigated. Elemental composition, electrical conductivity, surface functional groups and other parameters that could be highly relevant to electrochemical performances were carefully correlated.

2. Experimental

2.1 Materials

D-(+)-Glucose (≥99.5%) [CAS number: 50-99-7], D-(+)-glucosamine hydrochloride (≥99%) [CAS number: 66-84-2], iron(II)

sulfate heptahydrate ($FeSO_4 \cdot 7H_2O$, ACS reagent, ≥99.0%) [CAS number: 7782-63-0], polytetrafluoroethylene (60 wt% dispersion in H_2O) [CAS number: 9002-84-0], 2-propanol (≥99.8%) [CAS number: 67-63-0] were supplied by Sigma-Aldrich. Potassium hydroxide pellets (AnalaR NORMAPUR® Reag. Ph. Eur. analytical reagent) [CAS number: 1310-58-3] were obtained from VWR. Nickel meshes were purchased from Goodfellow. All chemicals were used as received.

2.2 Sample preparations

Solutions of HTC-D-(+)-glucose (abbreviated as HTC-G) and HTC-D-(+)-glucosamine hydrochloride (abbreviated as HTC-GA) were prepared by dissolving the sugars in hot deionized water; amounts and additives are presented in Table 1. Typically, half of the volumes prepared were transferred and sealed in Teflon-lined stainless steel autoclaves (200 mL capacity). Then the autoclaves were heated at a temperature of 200 °C for 24 h. After the hydrothermal treatment, the autoclaves were cooled down in air by natural convection. The solid HTC-sugars were recovered by filtration, washed with deionized water and dried at 110 °C.

The HTC-sugars were chemically activated by using KOH in three steps. First, the HTC-sugar was impregnated with a KOH solution (0.5 g mL^{-1}; weight ratio of KOH : HTC = 4 : 1) under constant stirring at room temperature overnight. Second, the mixture was dried in an oven at a temperature of 150 °C. Third, the dried and grounded mixture was thermally treated (activation) in a custom-made stainless steel reactor,[36] which was placed in a vertical tube furnace. The temperature was increased at a rate of 10 °C min^{-1} from room temperature to the set temperature (600, 700 or 800 °C) and held there for four hours (or otherwise stated), after which the reactor was cooled down in the protective nitrogen flow (200 standard cubic centimeters per minute) used during the activation. The ACs were washed with hot deionized water until the supernatant became pH neutral and then dried at 110 °C.

2.3 Materials characterization

The textural properties of the HTC-sugars and the corresponding ACs were studied by analyzing the volumetric N_2 and CO_2 adsorption–desorption isotherms recorded at −196 and 0 °C with a Micromeritics ASAP 2020 Physisorption Analyzer. Samples were degassed under dynamic vacuum conditions at temperatures of 200 (HTC-sugars) or 300 °C (ACs) for 10 h. The S_{BET} were calculated from the N_2 adsorption isotherms. Appropriate ranges of the relative pressure (p/p_0) were selected to ensured positive line intersects in the multipoint BET regression analysis ($C > 0$), and that the composite $V_{ads}(1 - p/p_0)$ increased with an increasing p/p_0.[49] The V_t was determined from the last point of adsorption isotherm at a $p/p_0 = 0.98$.

Table 1 Amount of starting materials for different hydrothermally carbonized sugars in 100 mL deionized water, with and without iron sulfate added

HTC codes	Type of sugar	Mass of sugar	$FeSO_4 \cdot 7H_2O$
HTC-GFe	D-(+)-Glucose	60 g (3.33 M)	2.5 g (0.09 M)
HTC-G	D-(+)-Glucose	60 g (3.33 M)	—
HTC-GAFe	D-(+)-Glucosamine HCl	50 g (2.32 M)	2.0 g (0.075 M)
HTC-GA	D-(+)-Glucosamine HCl	50 g (2.32 M)	—

The micropore volumes and surface areas were calculated with *t*-plot ($V_{\mu p\text{-}t}$ and $S_{\mu p\text{-}t}$) and DR ($V_{DR\text{-}N_2}$ and $S_{DR\text{-}N_2}$) methods using N_2 adsorption data. The carbon black statistical thickness method (STSA) was used for the *t*-plot analysis. Mesopore volumes and surface areas were determined by the *t*-plot and Barrett–Joyner–Halenda (BJH, based on the desorption data) methods. The ultramicropore volume and surface area were calculated with the DR method using CO_2 adsorption data. Throughout this manuscript, ultramicroporosity is defined as porosity with pore width less than 1 nm (predominantly 0.4–0.8 nm), accessible by CO_2 molecules at 0 °C.

The average micropore width, L_o, was calculated from the characteristic energy (E_o) as determined by the DR method using the equation: L_o (nm) = 13.7/(E_o − 9.7 kJ mol^{-1}).[50] The average pore diameter L_t was estimated by $4V_t/S_{BET}$. The PSDs were calculated from N_2 adsorption data using a nonlocal density functional theory (NLDFT) and carbon slit pores.

Elemental analysis of the samples was performed by the commercial company MEDAC Ltd., UK. CHN (or CHNS for some samples) composition was determined by conventional combustion analysis, while K and Fe were analyzed with a Varian Vista MPX ICP-OES system. X-ray diffraction (XRD) patterns were recorded on a Panalytical X'pert Pro alpha1 powder diffractometer in θ–2θ geometry and equipped with a Pixel detector and using a Cu-Kα_1 radiation (λ: 1.5406 Å). A Perkin Elmer TGA7 was used for thermogravimetric analysis of the mass change on increasing the temperature from 20 to 900 °C at a rate of 10 °C min^{-1} in a flow of oxygen (a platinum cup was used). The Raman spectra were recorded by using a Horiba LabRAM HR 800 Raman spectrometer with Nd:YAG laser (532 nm/50 mW). Scanning electron microscope (SEM) images were recorded with a JEOL JSM-7000 F microscope using accelerating voltages of 5 kV. TEM were recorded with a JEOL field-emission electron microscope (JEM-2100F) operated at 200 kV, equipped with Gatan Ultrascan 1000 and Orius 200D camera. High-angle annular dark-field STEM (HAADF-STEM) images and electron energy-loss spectroscopy (EELS) spectra were acquired by JEOL ADF detector and Gatan Image Filter (GIF Tridium), respectively. The TEM specimen was prepared by dispersing a small amount of the carbon powder in ethanol. The slurry was then deposited on Cu supporting grid with holey amorphous carbon films.

For X-ray photoelectron spectroscopy (XPS), a Kratos AXIS Ultra^{DLD} spectrometer (Kratos Analytical, Manchester, UK) was used. Samples were analyzed in a monochromatic Al-based X-ray with an analysis area of ~1 mm^2 (most of the signal was from an area of 700 × 300 μm). Then the relative surface compositions (in atomic%) were obtained from quantification of detailed spectra recorded for each element. All spectra have been adjusted based on the binding energy for the carbon peak at 285.0 eV. For carbon quantification from C 1s spectra, care has been taken to subtract the overlapping K 2p peaks.

2.4 Electrochemical studies

The electrochemical behavior was studied with a Bio-Logic SP-50 potentiostat using a spring-loaded symmetrical two-electrode cell (ECC-Std electrochemical cell from EL-Cell GmbH). The electrodes were composed of 70 wt% active material (ACs), 15 wt% polytetrafluoroethylene (PTFE) and 15 wt% acetylene black. Dropwise, 2-propanol was added to the electrode composite, and the mixture was homogenized for 15 minutes with agate mortar and pestle. The paste was spread on a Ni mesh, dried, and immersed in an aqueous solution of KOH (6 mol dm^{-3}) for at least one day to ensure a complete impregnation with the electrolyte. The loading of ACs per electrode was 5–8 mg cm^{-2}. A laboratory qualitative filter paper (Munktell) was used as a separator.

All the electrochemical studies were carried out at room temperature using a 6 M KOH electrolyte. Cyclic voltammetry (CV) and chronopotentiometry (CP) were performed in the voltage range of 0 to 1.0 V. The specific capacitance (C_m) was calculated based on two methods:

(i) CV, according to the following equation:

$$C_m = 4\frac{\int I(V)\mathrm{d}V}{mR\Delta V}$$

where $I(V)\mathrm{d}V$, m, R, ΔV are the integral area under the CV curve, the mass of active material (AC), scan rate, voltage range, respectively.

(ii) CP (discharge curve), according to the following equation:

$$C_m = 4\frac{I\Delta t}{m\Delta V}$$

where I, Δt, m, ΔV are the applied current, discharge time, the mass of active material (AC), and the voltage range, respectively.

2.5 Measurement of the electrical conductivity

The electrical conductivity was measured in a purpose-built pressure cell as shown in Fig. S1 (ESI†). The cell consists of a ceramic die, and a stationary and moveable piston made of stainless steel having a diameter of 11.9 mm. The cylindrical hole of the die is 12.0 mm in diameter and the close fit creates the pressure cell. The ceramic die thus provides insulation in-between the piston and the stationary piston during measurement of the electrical conductivity.

For the sample preparation, the stationary piston was placed in the die, in which the powder of AC was introduced, and the pressure cell was created by the movable piston. Pressure was applied with a Zwick universal testing machine, with a load capacity of 100 kN, and the sample was compressed stepwise with thresholds of 0.5, 2 and 7 MPa.

The DC resistance was recorded using a 4-probe micro-ohm meter Ken-MR300CA from Schuetz Messtechnik GmbH at the threshold pressure values, and once the pressure reached 7 MPa, the resistance was measured immediately and also after 1, 5 and 10 min. The conductivity was calculated based on the resistance value measured at 7 MPa after 10 min using the basic relationship $\sigma = l/AR$, where l represents the powder column height, obtained by the displacement of the piston, and A is the cross-section area of the piston.

Several reference measurements of the empty cell were made and the empty cell was found to have a resistance of 12–15 milliohm. Usually, the resistances of the compacted ACs powders were 10–50 times higher than this value. The empty-cell contribution was removed from the final data.

3. Results and discussion

3.1 Yields and compositions of HTC-G(Fe) and HTC-GA(Fe)

The yields and elemental compositions of HTC-G(Fe) and HTC-GA(Fe), with and without iron sulfate in the synthesis mixtures, are presented in Table 2. The yields of the HTCs were not influenced significantly with the addition of $FeSO_4 \cdot 7H_2O$. As expected, nitrogen atoms remained in HTC-GA and HTC-GAFe (6–8 wt% N). When comparing the compositions of the HTC-G and HTC-GFe, the addition of $FeSO_4 \cdot 7H_2O$ did not change the CHO elemental content. Besides, only a small amount of iron was included in HTC-GFe and HTC-GAFe. Here, note that the total elemental amounts of HTC-GA(Fe) did not sum up to 100%, they reached only 85–90%, which showed that their combustion was incomplete. This difficulty for combustion was also supported by TGA, which showed that HTC-GA was more difficult to combust than HTC-G (see Fig. S2 in ESI†). After the recovery by filtration and drying, the HTC-G and HTC-GFe could easily be ground to powder, while HTC-GA and HTC-GAFe were hard and difficult to grind.

3.2 Textural properties of KOH-ACs prepared from different precursors and additives

3.2.1 ACs from HTC-GFe and HTC-G: effect of the activation temperature. The activation temperature has been shown to affect the textural properties of KOH-activated ACs.[51,52] Hence, we varied the activation temperature from 600 to 800 °C, to control the porosity and surface area of the ACs (Table 3). On increasing activation temperature, the S_{BET} of the AC-GFe series increased from 1080 to 2260 $m^2\ g^{-1}$ and for the AC-G series from 880 to 1550 $m^2\ g^{-1}$; the external (S_{ext}) and mesopore surface area ($S_{mp\text{-}BJH}$) also increased. The AC-G series showed consistently lower surface areas than the AC-GFe series.

A high activation temperature has been shown to promote the formation of mesopores for KOH-ACs,[47,52] which we also observed. The AC-GFe-600 and AC-GFe-700 had N_2 isotherms (Fig. 1a and c) typical for micropores (type 1),[53,54] and narrow

Table 2 Bulk chemical composition of hydrothermally carbonized sugars (HTC-sugars) with and without iron sulfate added

		Elements (wt%, dry basis)					
HTC	Yield (%)	C	H	N	S	O	Fe
HTC-GFe	47	65.21	4.54	—	—	29.97	0.18
HTC-G	44	66.21	4.27	—	—	29.98	—
HTC-GAFe	38	60.95	4.63	6.47	0.97	16.18	0.59
HTC-GA	40	56.91	4.97	7.82	—	14.86	—

Table 3 Textural properties of ACs: (a) surface areas and (b) pore volumes and pore sizes calculated by different methods based on N_2 and CO_2 adsorption–desorption isotherms. Activated carbon (AC-X-*Y*) from hydrothermally carbonized glucose or glucosamine with and without iron (X: G, GA, GFe, or GAFe) prepared at temperatures of *Y*: 600–800 °C for 4 h (except 2 h for AC-GFe-800-2h)

(a)

	Surface area (m^2 g^{-1})					
AC samples	S_{BET}	$S_{DR\text{-}N_2}$	$S_{DR\text{-}CO_2}$	$S_{\mu p\text{-}t}$	S_{ext}	$S_{mp\text{-}BJH}$
AC-GFe-600	1080	1150	700	1025	55	50
AC-GFe-700	1690	1810	1060	1635	55	50
AC-GFe-750	2050	2130	1055	1910	140	130
AC-GFe-800-2h	2410	2500	1130	2190	220	165
AC-GFe-800	2260	2250	765	1940	320	230
AC-G-600	880	935	840	845	35	30
AC-G-700	1300	1380	1160	1250	50	40
AC-G-800	1550	1610	825	1415	135	125
AC-GAFe-600	1715	1820	1070	1620	95	80
AC-GAFe-700	2320	2300	770	2110	210	170
AC-GAFe-800	2355	2230	670	1965	390	350
AC-GA-600	1930	1990	960	1790	140	130
AC-GA-700	3000	2920	795	2540	460	375
AC-GA-800	3080	2990	640	1340	1740	1220
Norit SX ultra	985	1020	590	740	245	265

(b)

	Pore volume (cm^3 g^{-1})					Ave. pore size (nm)	
ACs	V_t	$V_{\mu p\text{-}t}$	$V_{mp\text{-}BJH}$	$V_{DR\text{-}N_2}$	$V_{DR\text{-}CO_2}$	L_t	L_o
AC-GFe-600	0.455	0.374	0.062	0.408	0.282	1.69	0.69
AC-GFe-700	0.679	0.596	0.055	0.643	0.426	1.60	0.77
AC-GFe-750	0.888	0.681	0.127	0.757	0.422	1.73	1.06
AC-GFe-800-2h	1.043	0.795	0.153	0.889	0.454	1.73	1.09
AC-GFe-800	1.026	0.668	0.196	0.799	0.306	1.82	1.23
AC-G-600	0.356	0.309	0.030	0.332	0.337	1.62	0.58
AC-G-700	0.520	0.455	0.043	0.489	0.466	1.61	0.64
AC-G-800	0.685	0.500	0.115	0.573	0.331	1.77	0.98
AC-GAFe-600	0.713	0.586	0.065	0.647	0.427	1.66	0.97
AC-GAFe-700	1.003	0.721	0.138	0.816	0.307	1.73	1.42
AC-GAFe-800	1.089	0.588	0.259	0.793	0.267	1.85	1.36
AC-GA-600	0.830	0.627	0.101	0.707	0.386	1.72	1.09
AC-GA-700	1.368	0.780	0.282	1.037	0.319	1.82	1.53
AC-GA-800	1.704	0.192	0.920	1.063	0.257	2.21	2.06
Norit SX ultra	0.743	0.271	0.461	0.364	0.238	3.02	1.07

PSDs with peaks at 8 and 11 Å (Fig. 1e). The AC-GFe-800 and AC-G-800, on the other hand, displayed additional mesopores (compare PSDs in Fig. 1e and f). Distinctively, AC-GFe-800 and AC-G-800 had additional pores in the range of 15 to 30 Å. The AC-GFe-750 exhibited a transitional PSD type between AC-GFe-700 and AC-GFe-800.

The transition between PSD types can be rationalized from the reactions of KOH with the carbon precursor mixture at elevated temperature (see ref. 28 for details on the mechanism of KOH activation). In brief, the massive release of various gaseous species above 700 °C, etches the carbon framework together with various potassium compounds. It also potentially contributes to intercalation of metallic K into the carbon lattices.[55] At these high temperatures, ACs with comparably large pores are formed, as is shown by our experiments.

The ultramicroporosity (as probed by CO_2 sorption) showed a maximum with respect to the activation temperature for both the AC-GFe and AC-G series. The highest ultramicropore area ($S_{DR\text{-}CO_2}$) was reached at the intermediate activation temperature of 700 °C. Both AC-GFe-700 and AC-G-700 had a high $S_{DR\text{-}CO_2}$ of 1000–1200 m^2 g^{-1} and a high ultramicropore volume ($V_{DR\text{-}CO_2}$) of 0.42–0.47 cm^3 g^{-1}, while the ACs formed at 800 and at 600 °C had significantly lower $S_{DR\text{-}CO_2}$ and $V_{DR\text{-}CO_2}$ (Table 3). In other words, a high activation temperature of 800 °C mainly contributed to a high pore volume in the range of wider micropore (>1 nm) and small mesopores (2–3 nm).

3.2.2 ACs from HTC-GFe activated at 800 °C: the effect of activation time. The effect of activation time on the textural properties of ACs prepared by KOH activation was studied briefly. AC-GFe-800-2h (activated for 2 h) displayed a much higher ultramicropore volume than AC-GFe-800-4h (activated for 4 h). This difference can be qualitatively observed in Fig. 2a, where the AC-GFe-800-2h had a significantly higher uptake of CO_2 than the AC-GFe-800-4h. The prolonged activation appears to have enlarged the pores *via* kinetic contributions of the related activation chemistry.

The N_2 isotherms of AC-GFe-800-2h and AC-GFe-800-4h were, on the other hand, almost identical as shown in the Fig. S3,† and the S_{BET} and V_t of AC-GFe-800-2h (2414 m^2 g^{-1} and 1.043 cm^3 g^{-1}) were only slightly higher than those of AC-GFe-800-4h (2260 m^2 g^{-1} and 1.026 cm^3 g^{-1}). The AC-GFe-800-2h showed a higher pore volume at the pore width of <10 Å than AC-GFe-800-4h. Meanwhile, AC-GFe-800-4h showed a higher pore volume at the pore width of 15–35 Å than AC-GFe-800-2h (Fig. 2b). The higher surface area and pore volume of AC-GFe-800-4h in the range of wider micropore and mesopore were confirmed by *t*-plot and BJH analysis (Table 3).

3.2.3 ACs from HTC-GA(Fe): effect of the activation temperature. As for the AC-GFe and AC-G series, the surface area for AC-GAFe and AC-GA increased with an increased activation temperature. The AC-GAFe series had S_{BET} values in the range of 1716 to 2355 m^2 g^{-1} (V_t from 0.7 to 1.1 cm^3 g^{-1}) and the AC-GA in the range of 1930 to 3085 m^2 g^{-1} (V_t from 0.8 to 1.7 cm^3 g^{-1}) (Table 3 and Fig. 3). These surface areas superseded significantly those reported previously. In an earlier study of KOH-ACs prepared from HTC-GA, Zhao *et al.* obtained ACs with S_{BET} of 600 m^2 g^{-1}.[31] At similar activation conditions, *i.e.* with same KOH : HTC ratio, activation temperature and duration, our equivalent ACs showed S_{BET} values of 1716 (AC-GAFe-600) and 1930 (AC-GA-600) m^2 g^{-1}, presenting an impressive three-fold increment. This marked improvement is probably due to a better mixing of KOH and HTC-GA (or HTC-GAFe) by the wet impregnation method as compared to the physical mixing used in ref. 31.

Interestingly, the AC-GA-600 and AC-GAFe-600 (Fig. 3e and f) displayed PSDs similar to AC-G-800 and AC-GFe-800 rather than the 600 series. Tentatively, we ascribe this change to the chemical difference of HTC-G and HTC-GA. As mentioned earlier, there are additional nitrogen-containing chemical groups (pyrrole-like molecules, amide bonds and aromatic

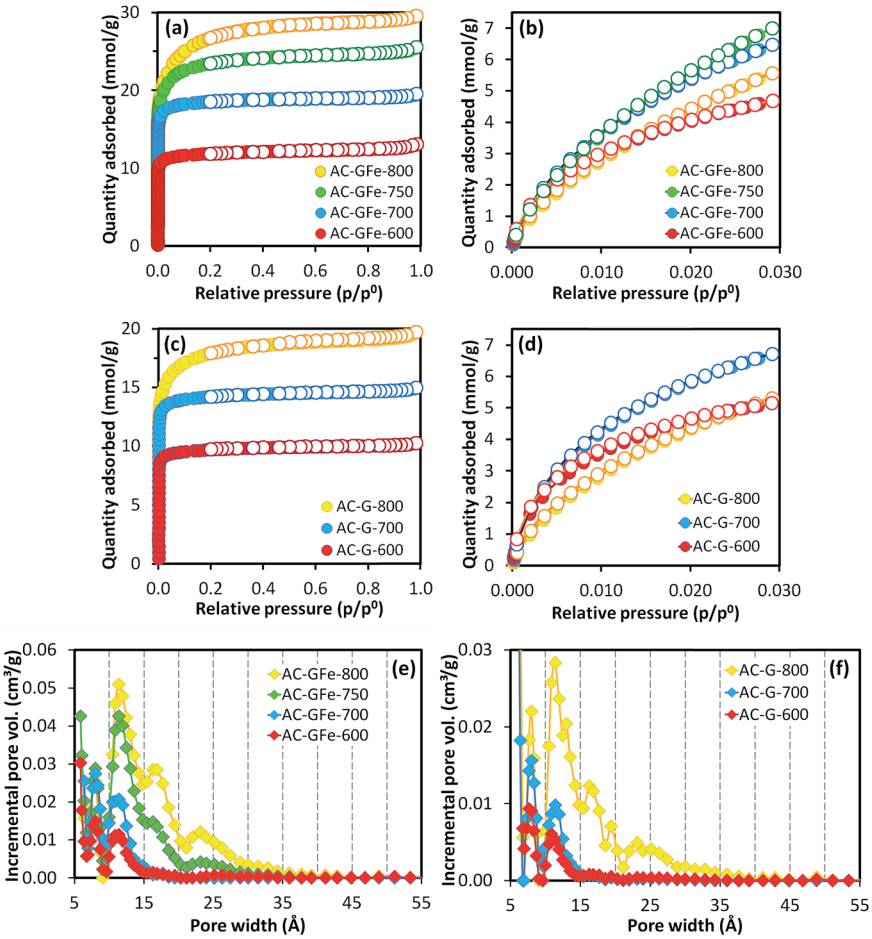

Fig. 1 (a and c) N_2 adsorption–desorption isotherms at −196 °C and (b and d) CO_2 adsorption–desorption isotherms at 0 °C for AC-GFe and AC-G series. The absolute pressure for CO_2 adsorption ranged from 0.3 to 102 kPa. Filled and empty symbols represent adsorption and desorption, respectively. Pore size distributions of AC-GFe (e) and AC-G (f) computed based on N_2 adsorption isotherm at −196 °C on carbon slit pores by NLDFT. All ACs were activated for 4 h. Activated carbons (AC-X-*Y*) from HTC-glucose with and without iron (X: G or GFe) prepared at temperatures of *Y*: 600–800 °C.

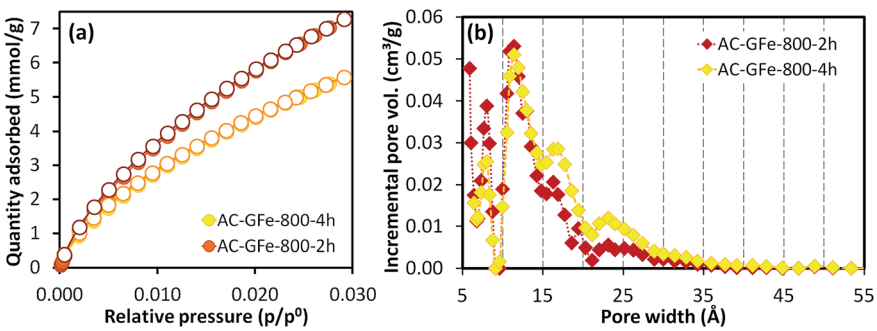

Fig. 2 (a) CO_2 adsorption–desorption isotherms at 0 °C for AC-GFe-800-2h and AC-GFe-800-4h, the absolute pressure for CO_2 adsorption ranged from 0.3 to 102 kPa; (b) pore size distributions show that AC-GFe-800-2h possesses higher ultramicropore (<1 nm) volume. Activated carbons (AC-X-*Y*) from hydrothermally carbonized glucose with iron (X: GFe) prepared at a temperature of *Y*: 800 °C.

amines) in HTC-GA.[15] Different amounts and types of gaseous species would be generated during the thermal treatment for HTC-G and HTC-GA, which appear to have led to a generation of porosity at a lower temperature for HTC-GA. Further investigations are required to fully understand the complicated reaction mechanisms occurring during the activation of HTC-GA and HTC-GAFe; however, these were not the main focus of this study.

Irrespective of the detailed mechanisms of activation, the AC-GA and AC-GAFe series demonstrated higher specific

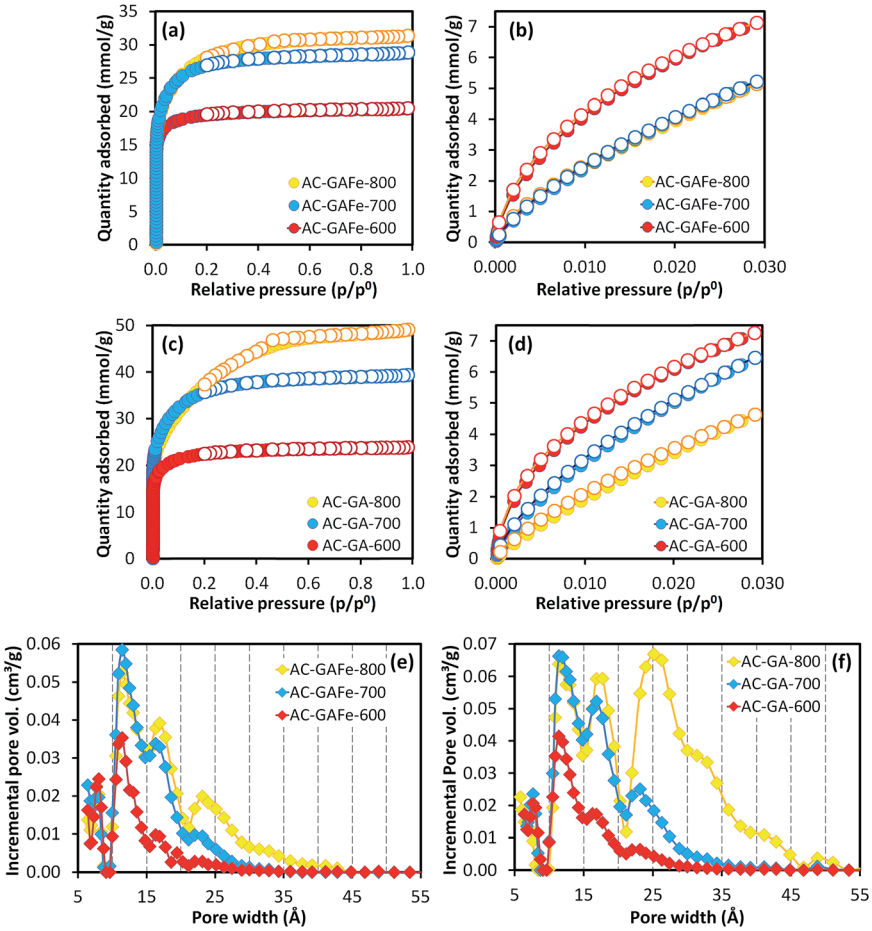

Fig. 3 (a and c) N_2 adsorption–desorption isotherms at −196 °C and (b and d) CO_2 adsorption–desorption isotherms at 0 °C for AC-GAFe and AC-GA series. The absolute pressure for CO_2 adsorption ranged from 0.3 to 102 kPa. Filled and empty symbols represent adsorption and desorption, respectively. Pore size distributions of AC-GAFe (e) and AC-GA (f) series computed based on N_2 adsorption data recorded at a temperature of −196 °C using a nonlocal density functional theory based on carbon slit pores. All ACs were activated for 4 h. Activated carbons (AC-X-*Y*) from hydrothermally carbonized glucosamine with and without iron (X: GA or GAFe) prepared at temperatures of *Y*: 600–800 °C.

surface areas and wider PSDs than the AC-G and AC-GFe series. From Table 3b, it is clear that the AC-GA and AC-GAFe series had larger average pore diameters (L_t) and average micropore widths (L_o) than the AC-G and AC-GFe series. As for the S_{BET}, the ultramicroporosity of the AC-GA and AC-GAFe series peaked at a lower activation temperature than for the AC-G and AC-GFe series. For the AC-GA and AC-GAFe series, the highest $S_{DR\text{-}CO_2}$ and $V_{DR\text{-}CO_2}$ occurred at 600 °C.

3.2.4 Roles of the $FeSO_4$ additive: AC-GFe *vs.* AC-G and AC-GAFe *vs.* AC-GA. The $FeSO_4$ additive affected the pore texture in both the AC-GFe and AC-GAFe but in different manners. For the AC-GFe, the S_{BET} was increased and the ultramicroporosity ($S_{DR\text{-}CO_2}$) was decreased as compared with the AC-G. For the AC-GAFe, the S_{BET} was decreased and the formation of wider microporosity and mesoporosity appeared to have been suppressed as compared with the AC-GA. These different tendencies may be interesting for further studies as the $FeSO_4$ additive could be used to control the porosity of AC in addition to the traditional manners.

3.3 Elemental composition of activated carbons

In the XPS analysis of selected ACs, wide (survey) spectra as shown in Fig. S4 and S5† were recorded to detect the elements of the surface layer of selected ACs. The shape of all high-resolved carbon spectra resembles that of carbon black. Detailed assignment of the bands was not possible due to different oxidation states indicated by the very long slope on the high binding energy side of the peaks in the spectra (Fig. S6 and S7†).

The carbon content and associated O/C atomic ratio decreased with an increased activation temperature for all the series of ACs. As shown in Table 4, the carbon content of AC-GFe-800-2h and AC-GA-800 was 90.6 and 91.8 at%, compared to 85.7 and 83.4 at% for AC-GFe-700 and AC-GA-700. Meanwhile, the oxygen content of AC-GFe-800-2h and AC-GA-800 was 7.8 and 6.1 at%, compared to 11.0 and 11.8 at% for AC-GFe-700 and AC-GA-700. The bulk elemental compositions of carbon and oxygen for the ACs are presented in Fig. S8,† which show a trend of increased carbon and decreased oxygen content on increased activation temperature. The AC-GA and AC-GAFe

Table 4 Relative surface elemental composition in atomic% calculated from XPS analysis

	Atomic%							
Sample	C	O	N	Fe	K	S	Si	Ni
AC-G-700	89.7	9.0	—	—	1.2	—	0.1	—
AC-GFe-700	85.7	11.0	—	1.4	1.6	0.1	(0.1)	(0.1)
AC-GFe-800-2h	90.6	7.8	0.4	0.2	0.8	0.1	(0.1)	—
AC-GA-700	83.4	11.8	1.5	0.3	3.0	<0.05	—	—
AC-GA-800	91.8	6.1	0.8	0.3	0.9	—	—	—
AC-GAFe-700	71.4	16.8	1.1	9.2	0.8	0.1	0.4	0.2

series contained 0.8–1.5 at% of N based on XPS analysis (Table 4). At a higher temperature, more nitrogen was released.

For the AC-GFe series (Fig. S9c†) and the AC-GAFe-600 (Fig. S9e†), the XRD patterns corresponded to Fe_3O_4 and Fe. However, only metallic Fe was observed for the AC-GAFe-700 and AC-GAFe-800. Unexpectedly, contamination by metallic Fe was detected in all other ACs. The origin of the Fe contaminants was the corrosion from the stainless steel mesh used in our reactor. To avoid Fe contaminants in future studies, a base-resistant nickel mesh is suggested. The metallic impurities can also be minimized by acid washing (*e.g.* HCl) after KOH activation.

3.4 Electrochemical studies

The electrochemical performance of the ACs was studied in a symmetrical two-electrode cell using a 6 M KOH electrolyte. The two-electrode cell mimicked the physical configuration, internal voltages and charge transfer that occur in real supercapacitor devices.[56] Consequently, it gives the best and most reliable indication of the performance of the ACs as electrode materials. A commonly available commercial AC, Norit SX Ultra, was used as a reference material and served as an internal validation of the electrochemical measurements (see Table 3 for textural properties).

Notably, all of the HTC-sugar-based ACs had higher specific capacitances (C_m) than Norit SX Ultra (Fig. 4 and Table 5) as determined by cyclic voltammetry (CV) and chronopotentiometry (galvanostatic charge–discharge studies) (Fig. S10† and Table 5). The maximum C_m values were determined at a low scan rate (2 mV s^{-1}) (Table 5), and the C_m decreased on increasing scan rates (up to 200 mV s^{-1}). At 2 mV s^{-1}, peak currents associated with oxidation at 1 V can be observed for all samples (Fig. 4 and 6). To evaluate the effect of the oxidation on the calculation of C_m, we also calculate the C_m using the voltage range from 0 to 0.90 V and 0 to 0.80 V. The values (Table S1†) show that the extent of oxidation does not significantly affect the C_m values; albeit the C_m values of samples AC-GA-600 and AC-GAFe-600 increased more significantly than other samples because of their lower capacitance in 0.9 to 1.0 V (to be discussed in the latter section). Furthermore, it was noted that the oxidation subsided on increasing scan rates. For instance, CV curves of sample AC-G-700 at different rates are presented in Fig. S11.†

Retaining the highest possible C_m at high scan rates (*i.e.* rate performance) is critical in developing supercapacitor electrodes[57–59] as it directly affects the power output. The best performers in this study retained 140–155 F g^{-1} at scan rates of 200 mV s^{-1} as shown in Table 5. At a low scan rate, the ions can effectively penetrate the pores and increase the number of charges in the EDL leading to a high C_m. For more rapid scan rates, the diffusion limitation of the electrolyte in the pores reduces the C_m.[60] Generally, the rate performance improved when activation temperature increased from 600 to 800 °C, where an increased activation temperature was shown to widen the PSD (Fig. 1e and f and 3e and f). Beside diffusion limitation, ohmic resistances of the electrolyte or the ACs can reduce the C_m.[30,60] Different electrical conductivities of the ACs (Fig. S13†) did not significantly impact the rate performance. This can be related to the electrode composition (70% AC: 15% carbon black: 15% PTFE). The high content of binder and conductive additive equalized the conductivities of the electrodes, thus limited the influence from the differential conductivity of the ACs.

The C_m of the AC-G and AC-GFe series were in the range of 200–260 F g^{-1}, and the highest C_m was recorded for those prepared at 700 °C: 241 F g^{-1} for AC-GFe-700 and 258 F g^{-1} for AC-G-700 (Fig. 4a and c). The values for C_m of the AC-G and AC-GFe series correlated with the ultramicropore parameters ($S_{DR\text{-}CO_2}$ and $V_{DR\text{-}CO_2}$) but not with the S_{BET} (Fig. 5). These tendencies are consistent with the findings of Vix-Guterl *et al.*, who showed that the C_m of templated porous carbons in both aqueous and organic electrolytes were proportional to the CO_2-based ultramicropore volume.[48] Besides, Raymundo-Piñero *et al.* showed an increasing efficiency of the pores in ACs for forming the EDLs in aqueous electrolytes of 6 M KOH or 1 M H_2SO_4 when pore size decreases from 1.4 to 0.7 nm.[47] In other words, the optimal pore size for ACs used with aqueous electrolytes is around 0.7 nm. The reason for the enhancement of capacitance in the region of ultramicroporosity was initially explained by Chmiola *et al.* The distortion of the ion solvation shell and partial removal of the ion solvation in the ultramicropores would reduce the distance between ion and carbon surface (also known as charge separation distance) and thus improve the electric double layer capacitance. As a result, the specific capacitance is correlated closely to ultramicroporosity probed by CO_2 adsorption.[44,61]

These findings support previous studies which have shown that the C_m of ACs do not correlate linearly with the S_{BET}, especially when the S_{BET} is higher than 1200–1500 m^2 g^{-1}.[1,62,63] On the contrary, a high C_m of ~260 F g^{-1} is achievable at a moderately high S_{BET} of ~1300 m^2 g^{-1} (AC-G-700), equivalent to C_m/S_{BET} of 20 μF cm^{-2}, which is among the highest value reported for undoped porous carbons. From an industrial perspective, a S_{BET} between 1000–1500 m^2 g^{-1} of ACs appears to be desirable.[64]

While the CV curve of the Norit SX Ultra exhibited an ideal rectangular shape, which is generally noticed for EDL capacitors with low internal resistance, the HTC-sugar derived ACs displayed slight deviations from the rectangular shape (Fig. 4). This deviation could be attributed to the oxygen rich nature of the ACs. Furthermore, the surface oxygen functional groups may have contributed to the increased responses of the current

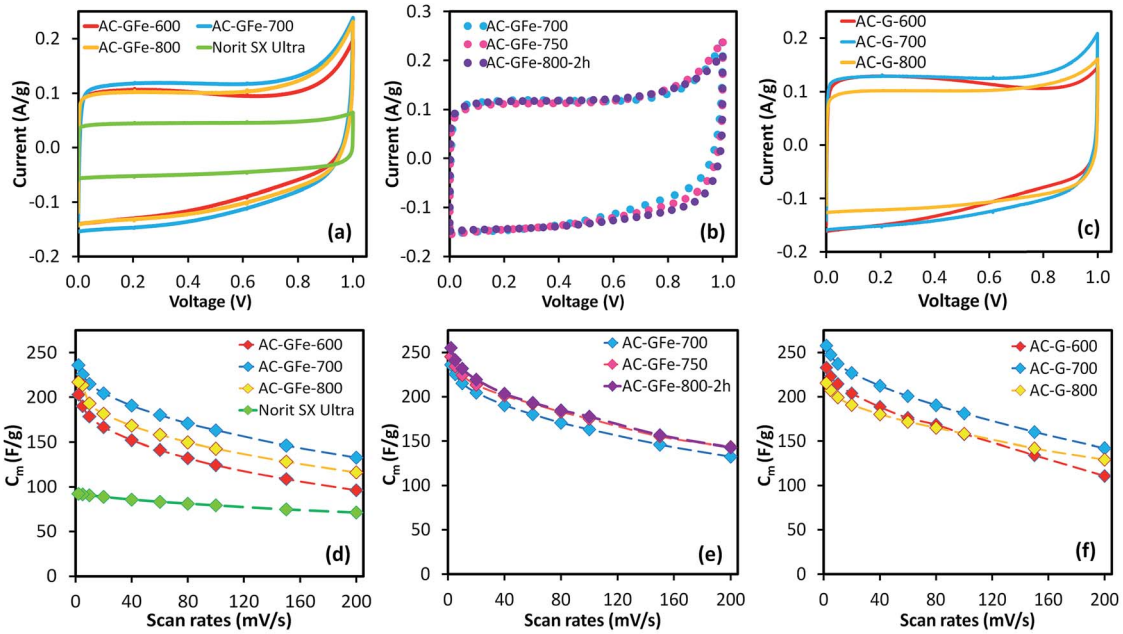

Fig. 4 (a–c) Cyclic voltammetry (CV) curves of AC-GFe and AC-G series at 2 mV s^{-1}, and (d–f) specific capacitances (C_m) calculated from CV scanned from 2 to 200 mV s^{-1}. Activated carbon (AC-X-Y) from hydrothermally carbonized glucose with and without iron (X: G, GA, GFe, or GAFe) prepared at temperatures of Y: 600–800 °C for 4 h (except 2 h for AC-GFe-800-2h).

Table 5 Specific capacitances (C_m) of prepared ACs in 6 M KOH, calculated from cyclic voltammetry (CV) and chronopotentiometry (CP; discharge curve). The rate performance is calculated based on [C_m (CV, 200 mV s^{-1})]/[C_m (CV, 2 mV s^{-1})] × 100%. Activated carbon (AC-X-Y) from hydrothermally carbonized glucose or glucosamine with and without iron (X: G, GA, GFe, or GAFe) prepared at temperatures of Y: 600–800 °C for 4 h (except 2 h for AC-GFe-800-2h)

	Specific capacitance C_m (F g^{-1})			
ACs	CV, 2 mV s^{-1}	CV, 200 mV s^{-1}	CP, 0.2 A g^{-1}	Rate performance (%)
AC-GFe-600	203	96	193	47%
AC-GFe-700	241	133	232	56%
AC-GFe-750	246	143	234	58%
AC-GFe-800-2h	255	143	240	56%
AC-GFe-800	217	116	208	54%
AC-G-600	233	111	227	48%
AC-G-700	258	142	247	55%
AC-G-800	215	129	204	60%
AC-GAFe-600	243	103	233	42%
AC-GAFe-700	251	112	242	45%
AC-GAFe-800	230	139	226	61%
AC-GA-600	215	120	203	56%
AC-GA-700	263	154	250	58%
AC-GA-800	226	131	214	58%
Norit SX ultra	92	71	84	77%

density when the voltage approached 1 V, which correlated with the hydrolysis of water.

The shape of the CV curves for AC-G-600 and AC-GFe-600 presented in Fig. 4a(i) and c(i) deviated significantly from the ideal rectangular shape. During the voltage cycling, a higher current was observed at low voltage (<0.4 V) but a comparably lower current was noticed at higher voltage (>0.4 V). This behavior is unconventional for EDL capacitance. A possible explanation could be an "ion-sieving" effect, which could occur when the sizes of electrolyte ions are larger than the pore openings.[65–67] However, we observed similar CV curves for AC-GA-600 and AC-GAFe-600 (Fig. 6a and b(i)), which have comparably larger pores (see Section 3.2) and hence it rules out the "ion sieving" effect in this case. Instead, the particular higher current responses at low voltage range could be assigned to pseudocapacitance derived from oxygen functional groups at the surface of the ACs prepared at 600 °C. These ACs have a considerably higher oxygen content (and lower carbon content) than the ACs prepared at higher temperatures (see Section 3.3). Such features in the CV curve were observed for graphene oxide (carbon with rich oxygen functional groups) in a comparative study of graphene (relatively "pure" carbon) and graphene oxide as electrode materials for supercapacitors.[68] A higher activation temperature ≥700 °C reduces the density of surface functionalities on the ACs and these ACs resemble ore closely to the rectangular-shaped CV of EDL capacitors.[30]

The cycle life of an electrochemical cell based on electrode AC-G-700 was evaluated by repeating CV scans at 100 mV s^{-1} over 0 to 1 V for 10 000 cycles (Fig. S14†). The calculated C_m derived from the CV curves at different cycles were normalized to the value of an earlier cycle (cycle 5) in Fig. S14.† The capacitance of the electrochemical cell increased slightly (3%) after 1000 cycles. After that, the value remained stable up to 10 000 cycles.

For the AC-GA and AC-GA-Fe series prepared from HTC-GA, the C_m were 215 to 263 F g^{-1} (*cf.* Fig. 6) but no clear-cut

correlations of the C_m with the $S_{DR\text{-}CO_2}$ or $V_{DR\text{-}CO_2}$ were observed (Fig. 7). Nonetheless, the optimum activation temperature with respect to the C_m (AC-GA and AC-GAFe series) was 700 °C. This optimum temperature can be rationalized with respect to several possible reasons *e.g.* the surface area, carbon content and electrical conductivity. When comparing the CV curves of AC-GAFe-600 and AC-GAFe-700 in Fig. 6a, the additional oxygen functional groups of AC-GAFe-600 appeared to contribute with additional pseudocapacitance in the low voltage range. However, that was not sufficient to compensate for the loss of EDL capacitance at the high voltage range. The lower carbon content and extremely low electrical conductivity (Fig. S13†) of AC-GA-600 and AC-GAFe-600 restricted their EDL formation although they possessed values of $S_{\mu p\text{-}CO_2}$ comparable to the best ACs in the AC-G and AC-GFe series. The AC-GA-700 and AC-GAFe-700 performed generally better than AC-GA-800 and AC-GAFe-800 albeit their similar values of S_{BET}.

The electrical conductivity of the AC-GA and AC-GAFe series were unexpectedly much lower than their AC-G and AC-GFe counterparts (Fig. S13†). As mentioned in the introduction, N-doping is widely reported as a strategy to enhance the electrical conductivity of carbon materials. The relatively low electrical conductivity of the AC-GA and AC-GAFe series can be correlated to the destruction of the structural order of the carbons (with corresponding very high S_{BET} up to 3000 $m^2\ g^{-1}$ and higher mesoporosity). In a similar manner, the N-doped ACs with mesoporosity prepared by Sevilla *et al.* possessed lower electrical conductivity (120–130 S m^{-1}) as compared with their undoped analogues (450–460 S m^{-1}).[24]

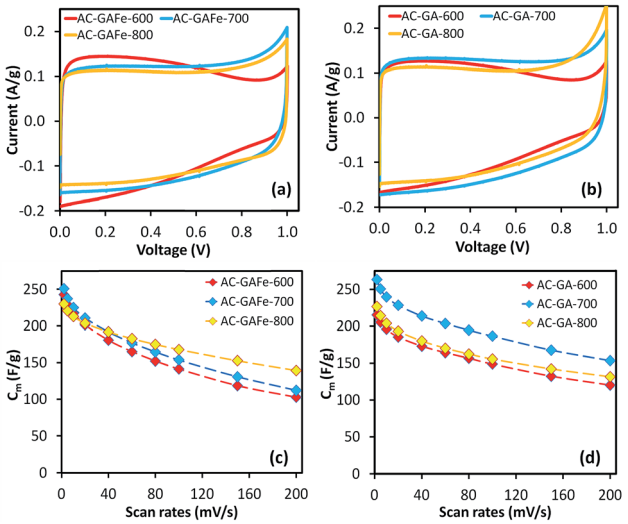

Fig. 6 (a and b) Cyclic voltammetry (CV) curves of AC-GA and AC-GAFe series at 2 mV s^{-1}, and (c and d) specific capacitances (C_m) calculated from CV scanned from 2 to 200 mV s^{-1}. Activated carbon (AC-X-*Y*) from hydrothermally carbonized glucosamine with and without iron (X: GA or GAFe) prepared at temperatures of *Y*: 600–800 °C.

Further optimization of AC-GA and AC-GAFe would be required (*e.g.* by lowering the KOH : HTC ratio) to more conclusively correlate the effect of porosity in the N-doped ACs to capacitances. The direction of the optimization would include preparing N-doped ACs with a narrow PSD but with different extent of ultramicroporosity, and ACs with similar surface area and pore volumes but with different average pore sizes and average micropore widths.

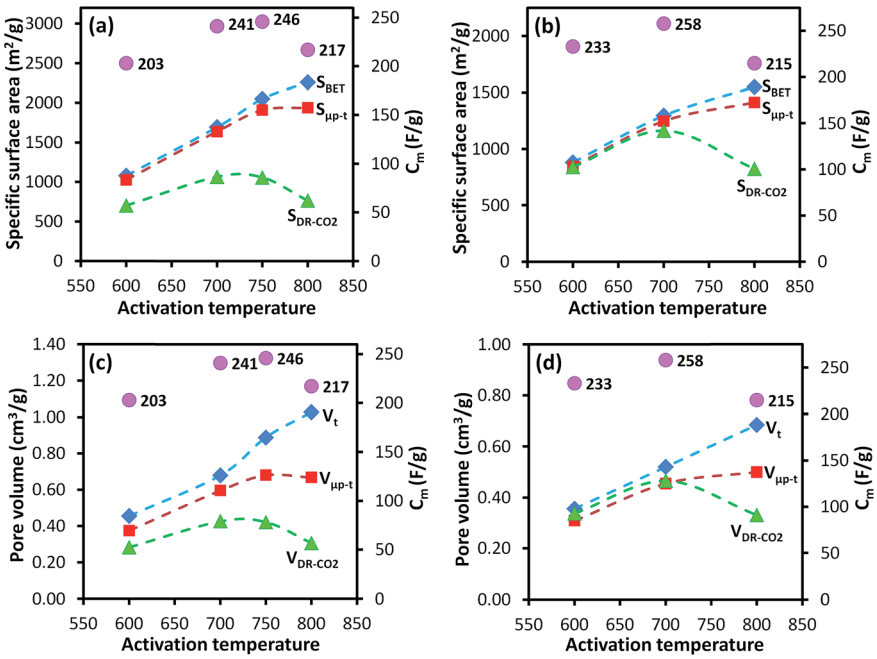

Fig. 5 Relationship between activation temperature *vs.* specific surface areas and pore volumes (dashed lines) calculated by various methods, and C_m (purple dots) for AC-GFe (a and c) and AC-G (b and d) series. Activated carbon (AC-X) from hydrothermally carbonized glucose with and without iron (X: G or GFe).

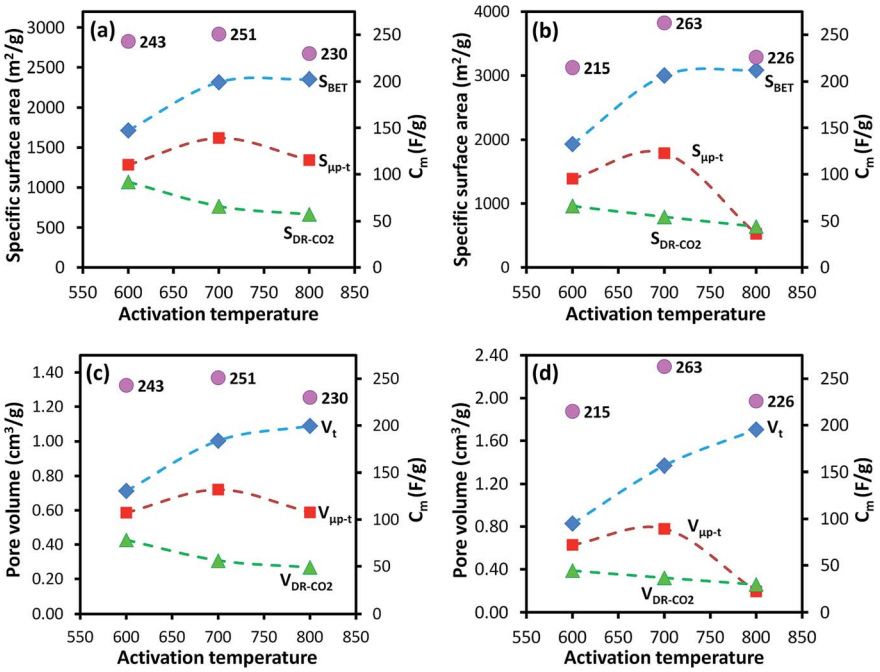

Fig. 7 Relationship between activation temperature *vs.* specific surface areas and pore volumes (dashed lines) calculated by various methods, and C_m (purple dots) for AC-GAFe (a and c) and AC-GA (b and d) series. Activated carbon (AC-X) from hydrothermally carbonized glucosamine with and without iron (X: GA or GAFe).

4. Conclusions

Textural properties (specific surface areas for different type of porosity, porosity from ultramicropores to supermicropores to mesopores) of ACs derived from HTC-G and HTC-GA could be finely tuned by changing the precursor mixtures and KOH-activation conditions (*e.g.* temperature, duration). All ACs were rich in oxygen functional groups, and the ACs derived from HTC-GA were enriched in nitrogen as well. This control opens up for further optimization of ACs derived from these and related precursors. The PSDs of AC-G(Fe) series were controlled by the activation temperature. At temperatures ≤700 °C, the ACs had narrow PSD with predominantly ultramicropores ($S_{\mu p\text{-}CO_2}/S_{BET} \approx$ 62–65%) and at >700 °C, larger pores ($S_{\mu p\text{-}CO_2}/S_{BET} \approx$ 30–52%) were formed due to the decomposition of K_2CO_3. The C_m of the AC-GFe and AC-G series in an aqueous electrolyte, 6 M KOH, correlated strongly with the ultramicroporosities that were probed by CO_2 physisorption. Albeit the surface specific capacitances in the highly porous ACs were very high (20 μF cm^{-2}), we foresee a strong need to further increase the rate capabilities of this kind of AC-based supercapacitor electrodes. By even higher activation temperatures the carbon content will be increased (lower O/C), and thus the electrical conductivity would be increased. It could certainly be relevant to further study the possibilities to increase the rate capabilities, while maintaining a high ultramicroporosity that appears to be a key to the function of carbon based EDL capacitors in aqueous electrolytes.

Acknowledgements

This project (No. 36912-2) was supported by the Swedish Energy Agency (Batterifondprogrammet). N. Hedin wishes to thank the award of postdoctoral fellowship (CTS 15:203) for K. K. Lee from the Carl Trygger Foundation for Scientific Research.

References

1 F. Beguin, V. Presser, A. Balducci and E. Frackowiak, *Adv. Mater.*, 2014, **26**, 2219–2251.
2 T. D. Atmaja and Amin, *Energy Procedia*, 2015, **68**, 429–437.
3 J. W. Long, *Electrochem. Soc. Interface*, 2008, **17**, 33.
4 J. R. Miller and A. F. Burke, *Electrochem. Soc. Interface*, 2008, **17**, 53–57.
5 A. Burke, *Int. J. Energy Res.*, 2010, **34**, 133–151.
6 A. Burke, *Electrochim. Acta*, 2007, **53**, 1083–1091.
7 S. Dietz and D. Recla, *Proceedings of the 14th International Seminar on Double Layer Capacitors and Hybrid Energy Storage Devices Florida*, 2004.
8 S. Dietz and D. Recla, US7541312 B2, 2009.
9 S.-E. Chun, Y. N. Picard and J. F. Whitacre, *J. Electrochem. Soc.*, 2011, **158**, A83–A92.
10 T. Thomberg, T. Tooming, T. Romann, R. Palm, A. Janes and E. Lust, *J. Electrochem. Soc.*, 2013, **160**, A1834–A1841.
11 M.-M. Titirici, R. J. White, C. Falco and M. Sevilla, *Energy Environ. Sci.*, 2012, **5**, 6796–6822.
12 M.-M. Titirici, R. J. White, N. Brun, V. L. Budarin, D. S. Su, F. del Monte, J. H. Clark and M. J. MacLachlan, *Chem. Soc. Rev.*, 2015, **44**, 250–290.

13 M. M. Titirici and M. Antonietti, *Chem. Soc. Rev.*, 2010, **39**, 103–116.
14 M. Sevilla, L. Yu, C. O. Ania and M.-M. Titirici, *ChemElectroChem*, 2014, **1**, 2138–2145.
15 L. Zhao, N. Baccile, S. Gross, Y. Zhang, W. Wei, Y. Sun, M. Antonietti and M.-M. Titirici, *Carbon*, 2010, **48**, 3778–3787.
16 X. Fan, C. Yu, Z. Ling, J. Yang and J. Qiu, *ACS Appl. Mater. Interfaces*, 2013, **5**, 2104–2110.
17 Z. Jinli, W. Jiao, L. Yuanyuan, N. Ning, G. Junjie, Y. Feng and L. Wei, *J. Mater. Chem. A*, 2015, **3**, 2043–2049.
18 J. Wu, C. Jin, Z. Yang, J. Tian and R. Yang, *Carbon*, 2015, **82**, 562–571.
19 Q. Wang, H. Li, L. Chen and X. Huang, *Carbon*, 2001, **39**, 2211–2214.
20 X. Sun and Y. Li, *Angew. Chem., Int. Ed.*, 2004, **43**, 597–601.
21 A. J. Romero-Anaya, M. Ouzzine, M. A. Lillo-Ródenas and A. Linares-Solano, *Carbon*, 2014, **68**, 296–307.
22 Y. Gong, H. Wang, Z. Wei, L. Xie and Y. Wang, *ACS Sustainable Chem. Eng.*, 2014, **2**, 2435–2441.
23 C. Falco, J. P. Marco-Lozar, D. Salinas-Torres, E. Morallón, D. Cazorla-Amorós, M. M. Titirici and D. Lozano-Castelló, *Carbon*, 2013, **62**, 346–355.
24 A. B. Fuertes and M. Sevilla, *ChemSusChem*, 2015, **8**, 1049–1057.
25 F. Gao, G. Shao, J. Qu, S. Lv, Y. Li and M. Wu, *Electrochim. Acta*, 2015, **155**, 201–208.
26 D. Salinas-Torres, D. Lozano-Castello, M. M. Titirici, L. Zhao, L. Yu, E. Morallon and D. Cazorla-Amoros, *J. Mater. Chem. A*, 2015, **3**, 15558–15567.
27 X. Zheng, W. Lv, Y. Tao, J. Shao, C. Zhang, D. Liu, J. Luo, D.-W. Wang and Q.-H. Yang, *Chem. Mater.*, 2014, **26**, 6896–6903.
28 J. Wang and S. Kaskel, *J. Mater. Chem.*, 2012, **22**, 23710–23725.
29 M. Olivares-Marín, J. A. Fernández, M. J. Lázaro, C. Fernández-González, A. Macías-García, V. Gómez-Serrano, F. Stoeckli and T. A. Centeno, *Mater. Chem. Phys.*, 2009, **114**, 323–327.
30 J. Sánchez-González, F. Stoeckli and T. A. Centeno, *J. Electroanal. Chem.*, 2011, **657**, 176–180.
31 L. Zhao, L. Z. Fan, M. Q. Zhou, H. Guan, S. Qiao, M. Antonietti and M. M. Titirici, *Adv. Mater.*, 2010, **22**, 5202–5206.
32 D. Hulicova-Jurcakova, M. Kodama, S. Shiraishi, H. Hatori, Z. H. Zhu and G. Q. Lu, *Adv. Funct. Mater.*, 2009, **19**, 1800–1809.
33 P. Burg, P. Fydrych, D. Cagniant, G. Nanse, J. Bimer and A. Jankowska, *Carbon*, 2002, **40**, 1521–1531.
34 D. Hulicova-Jurcakova, M. Seredych, G. Q. Lu and T. J. Bandosz, *Adv. Funct. Mater.*, 2009, **19**, 438–447.
35 G. Wang, J. Zhang, S. Kuang, J. Zhou, W. Xing and S. Zhuo, *Electrochim. Acta*, 2015, **153**, 273–279.
36 W. Hao, E. Björkman, Y. Yun, M. Lilliestråle and N. Hedin, *ChemSusChem*, 2014, **7**, 875–882.
37 X. Cui, M. Antonietti and S. H. Yu, *Small*, 2006, **2**, 756–759.
38 Q. Yan, J. Street and F. Yu, *Biomass Bioenergy*, 2015, **83**, 85–95.
39 K. K. Lee, S. Deng, H. M. Fan, S. Mhaisalkar, H. R. Tan, E. S. Tok, K. P. Loh, W. S. Chin and C. H. Sow, *Nanoscale*, 2012, **4**, 2958–2961.
40 K. K. Lee, R. W. Y. Ng, K. K. She, W. S. Chin and C. H. Sow, *Mater. Lett.*, 2014, **118**, 150–153.
41 J. Zhu, M. Chen, H. Qu, Z. Luo, S. Wu, H. A. Colorado, S. Wei and Z. Guo, *Energy Environ. Sci.*, 2013, **6**, 194–204.
42 L. Borchardt, M. Oschatz and S. Kaskel, *Mater. Horiz.*, 2014, **1**, 157–168.
43 O. Barbieri, M. Hahn, A. Herzog and R. Kötz, *Carbon*, 2005, **43**, 1303–1310.
44 J. Chmiola, G. Yushin, Y. Gogotsi, C. Portet, P. Simon and P. L. Taberna, *Science*, 2006, **313**, 1760–1763.
45 C. Largeot, C. Portet, J. Chmiola, P.-L. Taberna, Y. Gogotsi and P. Simon, *J. Am. Chem. Soc.*, 2008, **130**, 2730–2731.
46 J. Chmiola, C. Largeot, P.-L. Taberna, P. Simon and Y. Gogotsi, *Angew. Chem., Int. Ed.*, 2008, **47**, 3392–3395.
47 E. Raymundo-Piñero, K. Kierzek, J. Machnikowski and F. Béguin, *Carbon*, 2006, **44**, 2498–2507.
48 C. Vix-Guterl, E. Frackowiak, K. Jurewicz, M. Friebe, J. Parmentier and F. Béguin, *Carbon*, 2005, **43**, 1293–1302.
49 ISO 9277:2010, *Determination of the Specific Surface Area of Solids by Gas Adsorption—BET Method*, ISO, 2010.
50 F. Stoeckli, M. V. López-Ramón, D. Hugi-Cleary and A. Guillot, *Carbon*, 2001, **39**, 1115–1116.
51 D. Lozano-Castelló, M. A. Lillo-Ródenas, D. Cazorla-Amorós and A. Linares-Solano, *Carbon*, 2001, **39**, 741–749.
52 M. Sevilla, A. B. Fuertes and R. Mokaya, *Energy Environ. Sci.*, 2011, **4**, 1400–1410.
53 K. S. W. Sing, D. H. Everett, R. A. W. Haul, L. Moscou, R. A. Pierotti, J. Rouquerol and T. Siemieniewska, *Pure Appl. Chem.*, 1985, **57**, 603–619.
54 L.-C. Dolores, S.-G. Fabián, C.-A. Diego and L.-S. Ángel, in *Carbons for Electrochemical Energy Storage and Conversion Systems*, ed. F. Béguin and E. Frackowiak, CRC Press, 2009, pp. 115–162.
55 J. Romanos, M. Beckner, T. Rash, L. Firlej, B. Kuchta, P. Yu, G. Suppes, C. Wexler and P. Pfeifer, *Nanotechnology*, 2012, **23**, 015401–015407.
56 M. D. Stoller and R. S. Ruoff, *Energy Environ. Sci.*, 2010, **3**, 1294–1301.
57 R. Kötz and M. Carlen, *Electrochim. Acta*, 2000, **45**, 2483–2498.
58 A. Burke, *J. Power Sources*, 2000, **91**, 37–50.
59 A. Burke and M. Miller, *J. Power Sources*, 2011, **196**, 514–522.
60 E. Frackowiak and F. Béguin, *Carbon*, 2001, **39**, 937–950.
61 P. Simon and Y. Gogotsi, *Acc. Chem. Res.*, 2013, **46**, 1094–1103.
62 H. Shi, *Electrochim. Acta*, 1996, **41**, 1633–1639.
63 D. Qu and H. Shi, *J. Power Sources*, 1998, **74**, 99–107.
64 P. Azaïs, in *Supercapacitors: Materials, Systems, and Applications*, ed. F. Béguin and E. Frąckowiak, Wiley-VCH Verlag GmbH & Co., 2013, pp. 307–371.

65 L. Eliad, E. Pollak, N. Levy, G. Salitra, A. Soffer and D. Aurbach, *Appl. Phys. A: Mater. Sci. Process.*, 2006, **82**, 607–613.
66 E. Avraham, B. Yaniv, A. Soffer and D. Aurbach, *J. Phys. Chem. C*, 2008, **112**, 7385–7389.
67 M. Noked, E. Avraham, Y. Bohadana, A. Soffer and D. Aurbach, *J. Phys. Chem. C*, 2009, **113**, 7316–7321.
68 B. Xu, S. Yue, Z. Sui, X. Zhang, S. Hou, G. Cao and Y. Yang, *Energy Environ. Sci.*, 2011, **4**, 2826–2830.